Reusable high-entropy oxide environmental photocatalyst towards toxic Cr(VI) reduction with tailored bandgap via solution combustion synthesis

Mariappan Anandkumar[a*], Kannan P.K.[b], Shanmugavel Sudarsan[a], Uchaev D.A.[a], Trofimov E.A.[a]

[a]South Ural State University, Chelyabinsk 454080, Russian Federation

[b]Department of Physics, PSG Institute of Technology and Applied Research, Coimbatore, 641 062, India

Corresponding author: e-mail drmaksmile@gmail.com

Abstract:

The use of oxide photocatalysts for removing pollutants from the environment has always been regarded as a promising solution and has attracted considerable attention. The current study investigates the bandgap engineering of $(CeGdSmYZr)O_2$ high-entropy oxide nanoparticles synthesized through a simple solution combustion technique. Different fuel-to-oxidizer ratios such as 0.06, 0.08, 1, 1.2, and 1.4 have been used to synthesize high-entropy $(CeGdSmYZr)O_2$ oxide nanoparticles. Various characterization techniques including x-ray diffraction (XRD), field emission scanning electron microscopy (FESEM), transmission electron microscopy (TEM), UV-visible spectroscopy, surface area measurements, and photoluminescent spectroscopy (PL) were used to investigate the structural, morphological, optical, and luminescent properties. XRD results confirm the formation of single-phase fluorite oxide while the fuel-to-oxidizer ratio was found to have an impact on the bandgap and crystallite size. This tailoring of bandgap has been shown to reflect in the photocatalytic reduction of toxic Cr(VI). The results showed that the photocatalytic reduction of Cr(VI) was significantly enhanced with an increase in the fuel-to-oxidizer ratio and a Cr(VI) reduction of

99.14 % was achieved involving 2 ml of formic acid. As a result, the findings of this study could provide insights into the development of new high-entropy oxide photocatalysts for the efficient reduction of toxic Cr(VI).

Keywords:

High-entropy oxide; Bandgap engineering; Photocatalyst; Cr(VI) reduction; Solution combustion; Fuel-to-oxidizer ratio

1. Introduction:

The major portion of the earth is comprised of water that can be regenerated, disseminated, distributed, and transported. These characteristics collectively add to water's great value to people. The groundwater and surface water resources are crucial for a variety of activities, including cattle development, energy generation, forestry, farming, aquaculture, seafaring, recreation, and so forth. It is a remarkable gift from nature to humanity that must be preserved. Therefore, it is important to manage water resources responsibly and sustainably.

It is unfortunate that the fast-growing major industries including pharmaceuticals[1], pesticides[2], fertilizers[3], paper,[4] leather[5] pose a threat to the health and environment due to the release of toxic chemicals and heavy metals. It is important to note that toxic heavy metals released from the industries including Pb (II), Hg (II), Cd (II), and Cr (VI), even at very low concentrations, have the potential to disrupt normal metabolic processes[6-11]. Among them, heavy metal ion hexavalent chromium (Cr(VI)) is generated primarily from industrial processes such as electroplating, metal finishing, leather tanning, dyeing, and textile production. According to the World Health Organization (WHO), Cr (VI) is classified as a group 1 carcinogen[12]. Two types of oxidized chromium exist, namely hexavalent chromium (Cr(VI)) and trivalent chromium (Cr(III)), the latter being less toxic than the former[8, 13]. The

non-biodegradable characteristics of Cr(VI) in nature and its high mobility make it likely that Cr(VI) will be mutagenic and carcinogenic to all living organisms.

The removal of toxic Cr(VI) from wastewater has been an extremely critical task in this context. The removal of Cr(VI) from industrial wastewater can be accomplished using several methods, including photocatalysis, electrocoagulation, microfiltration, ion exchange, adsorption, and chemical precipitation[14-16]. Accordingly, it is generally considered that the reduction of hexavalent Cr(VI) to its nontoxic counterpart Cr(III) would be a feasible solution to this issue. Using a semiconductor-based photocatalyst, photocatalytic reduction overcomes many of the limitations associated with using traditional treatment methods[16, 17]. There is a high efficiency of photocatalytic reduction and a low energy use associated with this technology. Due to its low cost and ease of application, this process makes it quite attractive for the reduction of hazardous Cr(VI) to less toxic Cr(III)[8, 17].

For the photocatalytic treatment of heavy metals, such as Cr(VI), a number of semiconductor photocatalysts are being considered, including pristine oxides such as TiO_2, ZnO, CdS, and WO_3[16, 17]. Various strategies such as doping, and forming heterojunctions were followed to improve the performance of the photocatalyst. Despite this, the technology appears to have reached a saturation point in terms of creating a new photocatalyst, necessitating the exploration of alternative photocatalysts. This has led to a great deal of interest in high-entropy ceramics, due to their unique compositional and structural integrity in forming single-phase solid solutions[18]. A high-entropy material is composed of five or more primary elements which that been shown to possess exceptional optical properties and have the potential to perform a wide range of functional applications[8, 19-23]. Despite this, there has been a relatively limited use of high-entropy oxides in the field of photocatalysis, and further studies are needed to open potential research applications[18]. This is especially true in the field of wastewater treatment. In this regard, high-entropy ceramics are increasingly seen as an

attractive alternative to traditional photocatalysts, with the potential to provide improved performance.

In comparison to traditional nanomaterials, high-entropy oxides (HEO) offer a promising alternative due to their tailored bandgaps, which have been achieved by varying the composition of high-entropy oxides[8, 23, 24]. It has been demonstrated that compositional variation can be used to engineer the bandgap of high-entropy oxides. An improvement in photocatalytic properties was observed as a result of this[8]. Also, high-entropy oxides have a number of multi-functional applications, including photocatalysts, sensors, and as a candidate for light-emitting diodes[8, 20, 22, 23]. There is only one composition of high-entropy oxide nanomaterial used in all of the above applications, indicating the broad application possibilities of high-entropy materials. Additionally, it has been reported that $TiZrNbTaWO_{12}$ high-entropy oxides have 10 heterojunctions within the system, which improves the yield of oxygen during photocatalysis which emphasizes the importance of high-entropy materials[25].

A number of factors influence the photocatalytic activity of the photocatalyst, including bandgap, crystallite size, bandgap position, recombination rate, etc[26, 27]. It is important to note that the bandgap plays a key role in electron-hole pair generation, while the bandgap position determines the pathway of photocatalytic reaction of dyes or heavy elements[16]. Consequently, it is possible to alter the bandgap and band edge position of a photocatalyst either through doping or through the use of a composite, resulting in improved photocatalytic performance[28, 29]. The above two approaches implement composition variation. It will therefore be interesting to examine the bandgap tuning of a photocatalyst without altering its composition or forming heterojunctions. It simplifies not only the synthesis process but also reduces the number of elements involved in heterojunction formation.

To achieve this bandgap variation in the synthesis step, a simple combustion technique will be employed in the present investigation. Solution combustion is a versatile synthesis technique explicitly used for the synthesis of metal oxides[30, 31]. A key advantage of employing solution combustion technique is that the resulting oxides form a porous network, which increases the surface area. This increased surface area facilitates the formation of additional active sites improving efficient diffusion of heavy elements, eventually improving the photocatalytic activity. Additionally, solution combustion techniques can be used to generate materials with controlled porosity, which further enhances their catalytic activity. To achieve this, the fuel-to-oxidizer ratio (F/O) was optimized during the combustion step[31]. The use of combustion synthesis has been reported in the literature to tailor the bandgap by varying the F/O ratio[32]. It is therefore possible to engineer the band structure of high-entropy oxides with tuneable properties, which will be essential for applications such as photocatalysis.

As a consequence, we are very interested in understanding how the F/O ratio affects the bandgap of $(CeGdSmYZr)O_2$ via solution combustion synthesis. The obtained nanoparticles will then be used as a photocatalyst to reduce Cr(VI) to Cr(III) using a UV-light source. To have a complete understanding of the synthesized $(CeGdSmYZr)O_2$ oxide, several photocatalytic reaction parameters, such as the photocatalyst dose, the Cr(VI) concentration, and the hole scavenger were studied. As a result of this study, we aim to provide a guide for creating other oxides using high-entropy concepts that may have potential applications in a variety of different functional areas.

2. Experimental section

2.1. Materials and reagents

Cerium (III) nitrate hexahydrate ($Ce(NO_3)_3•6H_2O$, 99.9%), zirconium (IV) nitrate dihydrate ($Zr(NO_3)_2•2H_2O$, 99%), gadolinium (III) nitrate hexahydrate ($Gd(NO_3)_3•6H_2O$,

99.99%), samarium(III) nitrate hexahydrate ($Sm(NO_3)_3$•$6H_2O$, 99.9%), yttrium(III) nitrate hexahydrate ($Y(NO_3)_3$•$6H_2O$, 99.8%), glycine (NH_2CH_2COOH, 98.5%), and, formic acid (HCOOH, 95%) was purchased from China. All the materials were marked with the analytical grade and were used as received without any purification. The deionized (DI) water was used for the synthesis.

2.2. Synthesis of (CeGdHfYZr)O_2 oxide nanoparticles

A simple solution combustion technique was used to prepare high-entropy (CeGdSmYZr)O_2 oxide[33]. Respective metal nitrates (0.001 M of each metal cation with a total metal concentration of 0.005 M) and glycine were used as an oxidizer and fuel respectively. The calculated amounts of fuel (Table S1) and oxidizer were dissolved in a minimal amount of distilled water until a transparent solution was obtained. For example, the reaction equation occurring in the process for a F/O ratio of 1 can be represented as displayed in equation (1),

$$\frac{18}{5}\,Ce(NO_3)_3 + \frac{18}{5}\,Zr(NO_3)_2 + \frac{18}{5}\,Gd(NO_3)_3 + \frac{18}{5}\,Sm(NO_3)_3 + \frac{18}{5}\,Y(NO_3)_3 + 28\,C_2H_5NO_2 + 15O_2 \rightarrow 18(CeGdSmYZr)O_2 + 56\,CO_2 + \frac{252}{5}N_2 + \frac{446}{5}H_2O \quad (1)$$

The solution is then transferred in a pre-heated hot air oven at 130 °C until all the water gets evaporated resulting in a gel-like appearance. To initiate the combustion, the beaker containing the gel is kept on a hotplate maintained at a set temperature of 320 °C. This action leads to the combustion of gel resulting in a large evolution of gases transforming gel into a porous powder. The obtained powder is then calcined in a muffle furnace at 500 °C for 2 hours in order to eliminate unreacted fuel and carbon residues during the combustion step. The powders after the calcination step are then used as such for further characterization and photocatalytic investigations. The prepared (CeGdHfYZr)O_2 samples were named as HEC-0.6, HEC-0.8, HEC-1, HEC-1.2, and HEC-1.4 for the sample prepared from corresponding F/O ratio 0.6, 0.8, 1, 1.2, and 1.4 respectively.

2.3. Characterization

The crystallinity of the prepared HEO was investigated using XRD (Rigaku Ultima IV, Rigaku) using Cu-K_α radiation (λ = 1.54 Å) from 20-80° with a scan speed of 1° per minute. Rietveld refinement analysis was performed using the Fullprof program and the Williamson-Hall (W-H) analysis was done to assess the contribution of crystallite size and the lattice strain in xrd peak broadening. FESEM images were captured using a JEOL (JEOL JSM-7001F, JEOL) microscope operated at 20 kV. TEM image and SAED pattern were captured using a JEOL microscope (JEOL JEM-2100, JEOL) operated at an acceleration voltage of 175 kV. The optical properties were investigated using a UV-visible spectrophotometer (Shimadzu UV-2700) in both absorbance and reflectance modes. The elemental composition of the synthesized HEO was calculated using an inductively coupled plasma -optical emission spectrometer (ICP-OES 700 series, Agilent). Fourier-transform infrared spectroscopy (FTIR) studies were performed on the powders using Shimadzu IRAffinity-1S. Sample preparation for the FTIR studies involves the preparation of the pellet by mixing the powder photocatalyst and KBr (1:100 weight ratio). Data was collected in transmittance mode from 400-4000 cm^{-1}.

2.4. Photocatalytic reduction of Cr(VI)

The synthesized (CeGdHfYZr)O_2 nanoparticles were used to investigate the reduction of toxic Cr(VI). The photocatalyst setup consists of a glass beaker in which 50 ml of 50 ppm Cr(VI) solution was added. To the above solution, 10 mg/L catalyst and 500 µl of formic acid were added and stirred continuously in the dark to attain adsorption-desorption equilibrium. After 60 min of stirring in the dark, the solution was further irradiated using a UV-light (100 W) having a wavelength of 365 nm. In all the cases, the distance between the light source and the photocatalyst reaction solution was maintained at 50 mm. Aliquots are drawn from the reaction mixture at regular intervals, and centrifuged to separate the photocatalyst from the solution.

The supernatant solution was then analysed using a UV-visible spectrophotometer. The current study investigates a complete set of experimental variables such as the effect of photocatalyst concentration, Cr(VI) concentration, hole scavenger, recyclability, and stability of the photocatalyst.

3. Results and discussions

To understand the effect of fuel to oxidizer ratio on the phase and structural evolution of high-entropy $(CeGdSmYZr)O_2$ oxide, we have used glycine as a fuel. The combustion-synthesized high-entropy oxides prepared by varying F/O ratio was studied using an X-ray diffraction and its corresponding X-ray pattern was displayed in Fig. 1(a). All the samples prepared using various F/O ratios exhibit x-ray reflections similar to cubic fluorite structure (ICDD PDF card no: 01-073-6318)[8]. In addition, other reflections are not observed in all the synthesized samples other than cubic fluorite structure indicating the formation of a single-phase solid solution. To confirm the formation of single-phase high-entropy oxide of the synthesized powder, Rietveld refinement was performed on the x-ray patterns using a Fullprof program and the result is presented in fig. 1(b-f). It is evident that the x-ray patterns fit well with the cubic fluorite model (Fm-3m) confirming the single-phase solid solution. The x-ray fitting parameter using Fullprof software is presented in table 1. An observable x-ray peak shift towards lower angles is observed in the samples with increasing F/O ratio. As a result, the lattice parameter of the oxide increases with increasing the F/O ratio. For a fuel lean (0.6) condition, a lattice parameter of 5.366 □ is obtained, while a lattice parameter of 5.407 □ for fuel-rich (1.4) condition is calculated. In addition, the x-ray peak broadness increases with increasing F/O ratio which indicates the formation of smaller crystallite size at fuel-rich conditions. The possible reason for the small crystallite size with increasing F/O ratio is due to the excess fuel restricting the nucleation growth[34]. Similarly, at higher F/O ratios, a significant amount of carbon formation is observed which is evidenced by the nature of the resultant powders (Fig.

To explore the morphological structure of combustion-synthesized high-entropy $(CeGdSmYZr)O_2$ oxides, FESEM was performed and displayed in fig. 2. It is observed that all the high-entropy samples show a porous network of interconnected particles. This is due to the nature of the synthesis method used[36, 37]. In a solution combustion technique, a large volume of gases spontaneously evolve during the combustion step, resulting in the formation of pores between the nanoparticles creating a porous network, which are useful in catalysis applications[37]. Porous nanostructures increase the number of active sites for catalytic reactions and therefore improve the reaction kinetics by making industrial dyes and toxic metals more accessible.

Fig. 2: (a-e) FESEM image of high-entropy oxides prepared using different F/O ratios (0.6, 0.8, 1, 1.2, and 1.4 respectively).

HRTEM images were captured for the best-performing catalyst (HEC-1.4) to investigate the nature of nanoparticles in the nanometer scale which is displayed in fig. 3(a). The HRTEM images of the powder sample are visualized as tiny nanoparticles in agglomerated form. The average particle size of 2.6 nm (d-spacing = 0.33 nm) is obtained which is similar to the values calculated from the xrd pattern. In addition, the SAED pattern (Fig. 3(b)) was captured to check the crystal structure of nanoparticles. The SAED patterns form diffused rings and are indexed to (111), (200), (220), and (311) planes of cubic fluorite structure. The obtained results are in line with the xrd results confirming the formation of single-phase high-entropy oxides. The elemental composition estimated from the ICP-OES is presented in table S2. All the metal cations are present in near equimolar composition with a deviation attributed to the purity of the initial salts used.

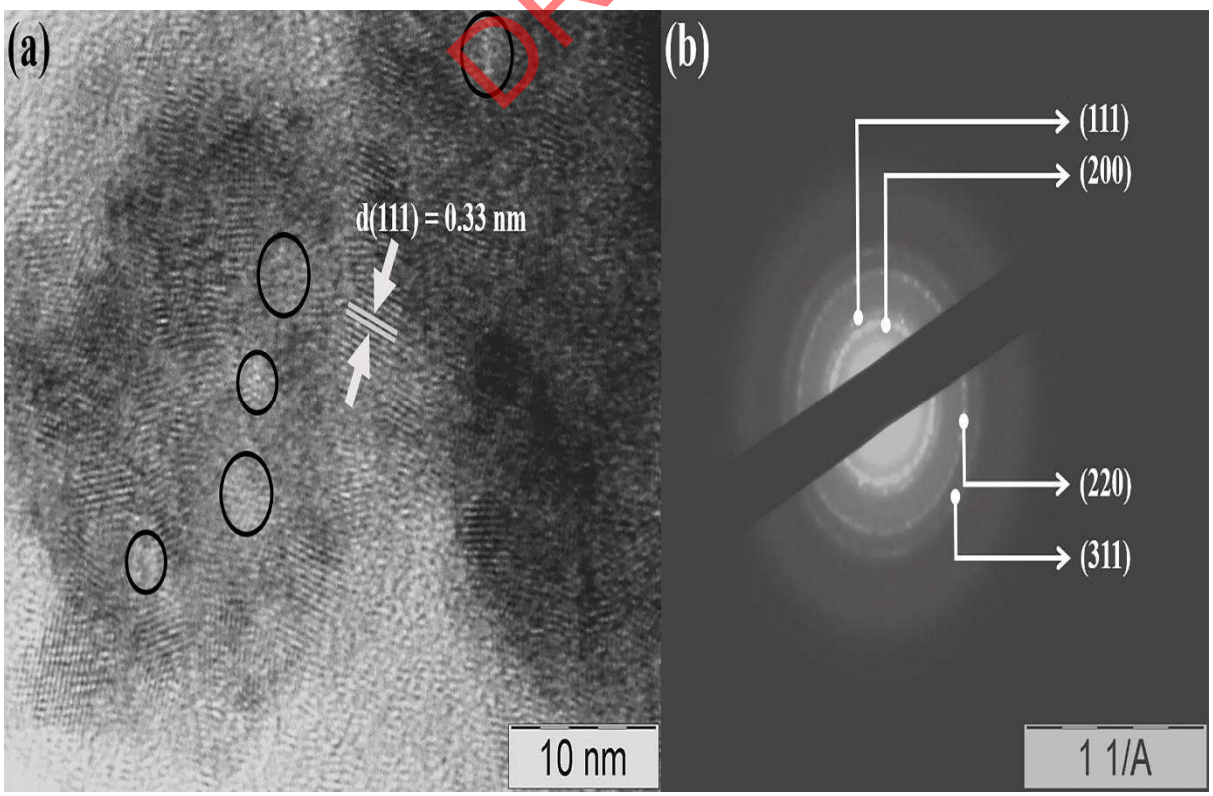

Fig. 3: (a) HRTEM image and (b) SAED pattern of HEC-1.4 powder. The black circles in the HRTEM image denote pores present as a result of combustion synthesis.

Photocatalytic performances are greatly influenced by the optical properties of the nanomaterials. Therefore, UV-visible spectroscopy is used to investigate the optical properties of high-entropy $(CeGdSmYZr)O_2$ oxides and the corresponding absorption spectra are displayed in fig. 4(a). The optical spectra of all the samples exhibit strong absorbance in the ultraviolet region which corresponds to the O^{2-} and $Me^{3+/4+}$ charge-transfer transitions[23]. The indirect bandgap energies of HEO were calculated using the Kubelka- Munk (K-M) function, F(R) by plotting hν versus $(F(R)* h\nu)^{(1/2)}$. The band gap values were calculated by extrapolating the linear part of the graph $(F(R)* h\nu)^{(1/2)} = 0$ as shown in fig.4(b). It was observed that with an increase in F/O ratio, the onset of absorption is blue-shifted, thereby increasing their bandgap. In semiconductor nanomaterials, the wavelength of the UV absorption edge is highly dependent on the particle size. Whenever the particle size is confined to the sub 10 nm scale, the band gap energy increases causing the absorption edge of the interband transition to be blue-shifted[23]. These results are in good agreement with the crystallite size calculated from the x-ray diffraction pattern (Table 1). Consequently, it is possible to tailor the optical bandgap by varying the synthesis conditions, and the synthesized HEO was further been employed as a photocatalytic material for the reduction of Cr(VI).

Table 1: Summary of various parameters calculated from Rietveld refinement, W-H plot, and UV-visible absorption spectra.

Sample	Size[a] (nm)	Lattice strain[a] (%)	Lattice parameter (Å)	Bandgap[b] (eV)	E_{VB} (eV Vs NHE)	E_{CB} (eV Vs NHE)

HEC-0.6	3.59	0.7	5.366 ± 0.001	3.08	2.519	-0.560
HEC-0.8	4.56	0.49	5.392 ± 0.0004	3.12	2.545	-0.574
HEC-1	3.19	0.69	5.376 ± 0.001	3.18	2.583	-0.596
HEC-1.2	2.94	0.87	5.373 ± 0.001	3.21	2.597	-0.612
HEC-1.4	2.68	0.75	5.407 ± 0.001	3.24	2.610	-0.629

[a] values obtained from Williamson-Hall plot

[b]calculated from K-M plot

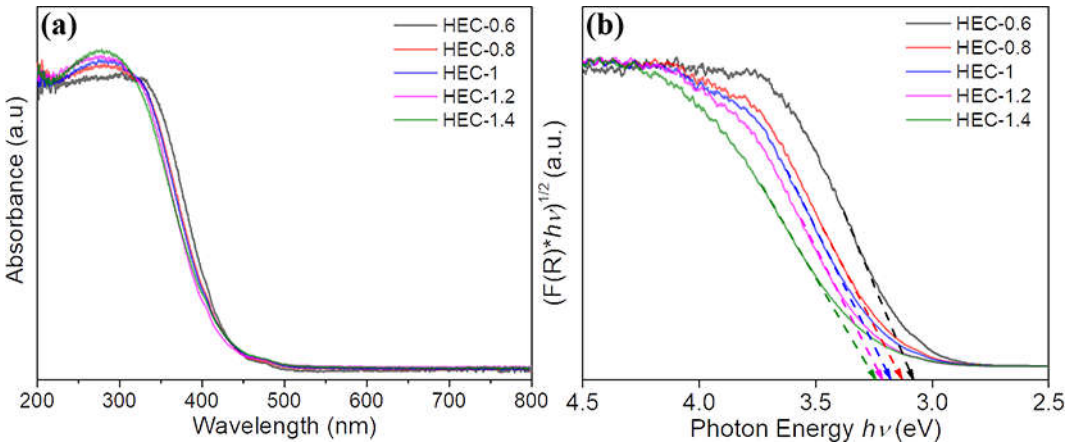

Fig. 4: (a) UV-visible spectra of high-entropy $(CeGdSmYZr)O_2$ oxides prepared using various F/O ratios via solution combustion and (b) its corresponding K-M plot to estimate the bandgap values.

The specific surface area measurements of synthesized photocatalyst was performed and the isotherm is displayed in fig. S3. Due to the nature of the pores created during the solution combustion synthesis, type IV BET isotherm is usually observed[38, 39]. The calculated specific surface area along with the pore volume and pore diameter is tabulated in Table S3. The sample HEC-1.4 has the larger surface area of 37.6 m^2/g and the lowest being HEC-0.6 with a surface area value of 32.1 m^2/g. This is due to the smaller crystallite size of HEC-1.4 compared to HEC-1.6 sample.

3.1 Photocatalytic reduction of Cr(VI) by $(CeGdSmYZr)O_2$ nanoparticles

To study the photocatalytic activity of high-entropy $(CeGdSmYZr)O_2$ oxide nanoparticles, Cr(VI) was selected as a model pollutant in the present investigation due to its toxic nature.

3.1.1 Effect of F/O ratio

The influence of F/O ratio on the photocatalytic performance of synthesized high-entropy $(CeGdSmYZr)O_2$ oxide on the reduction of Cr(VI) was evaluated and the UV spectra are presented in fig. S4 and $\ln(C_0/C)$ plots in fig. S5. Typically, the absorption spectrum shows an absorption maximum at 350 nm which indicated the presence of Cr(VI) species in the reaction. In the presence of UV-light illumination and photocatalyst, the peak absorption intensity of Cr(VI) gradually declined, indicating a decrease in the concentration of the heavy Cr(VI) metal. This is due to one electron transfer mechanism occurring in the photocatalytic reaction where Cr(VI) is reduced to Cr(III) [8, 40]. According to the Langmuir-Hinshelwood (L-H) model, the relationship between the initial Cr(VI) concentration and reduction rate explains the photocatalytic reaction kinetics. In general, it is the relationship between the degradation rate (r) and the concentration of reactants in water at a given time (C), which is expressed as (equation (2)),

$$r = -\frac{dC}{dt} = \frac{K_r K_{ad} C}{1 + K_{ad} C} \quad (2)$$

where K_r is the rate constant and K_{ad} is the adsorption equilibrium constant. When the concentration of the reactant is low, the reaction can be considered to be a first-order kinetic model and equation (1) is simplified as in equation (3),

$$ln\left(\frac{C_0}{C}\right) = K_r K_{ad} t = K_{app} t \quad (3)$$

where C_0 denotes the initial Cr(VI) concentration, and K_{app} is the rate constant.

Similarly, the Cr(VI) reduction efficiency at any time by the high-entropy $(CeGdSmYZr)O_2$ oxide photocatalyst was calculated from (equation (4)),

$$Cr(VI)\ reduction\ (\%) = \frac{[Cr(VI)]_0 - [Cr(VI)]_t}{[(Cr(VI)]_0} * 100 \quad (4)$$

where $[Cr(VI)]_0$ and $[Cr(VI)]_t$ represents the concentration of Cr(VI) at time 0 and time t respectively. Based on the obtained results (Fig. 5(a)), the performance of high-entropy oxide photocatalysts vary and show different kinetics of Cr(VI) reduction. The Cr(VI) reduction increases from 21.75 % to 36.25 % with samples prepared with increasing F/O ratios of 0.6 (HEC-0.6) and 1.4 (HEC-1.4) respectively (Fig. 5(b)). Photocatalysts prepared under fuel-rich conditions (HEC-1.4) show greater Cr(VI) reduction due to their smaller crystallite size. It is also evident from the BET measurements that HEC-1.4 has a larger surface area (table S3), and pore volume (0.118 cm^3/g) which further increases Cr(VI) adsorption facilitating faster reduction. For further studies on photocatalytic Cr(VI) reduction, the HEO sample prepared using F/O ratio of 1.4 was used (HEC-1.4). A control experiment was conducted in order to determine the necessity of a photocatalyst and an illumination source for a photocatalytic reaction to happen. Fig. S6 shows the absorption specta in the absence of photocatlysts and UV light source respectively. The results indicate that in absence of any one of the two, the reaction

was marginal highlighting the necessity of photocatalyt and UV-light source in the reduction of Cr(VI).

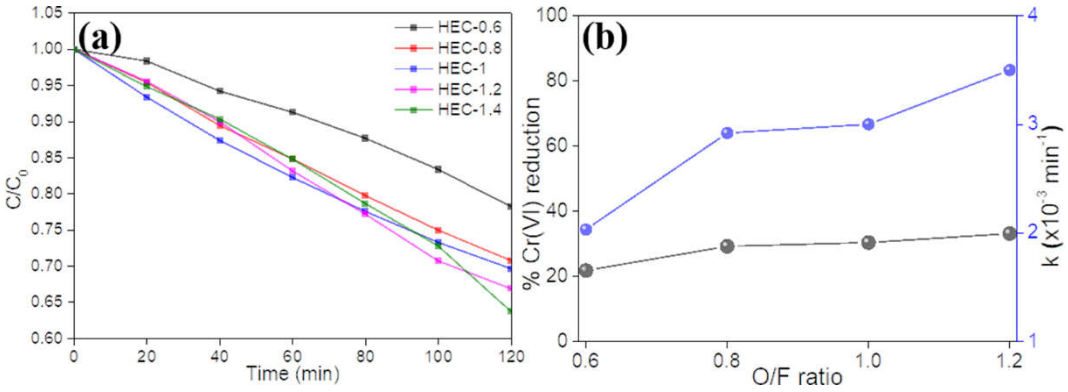

Fig. 5: (a) Plot of C/C_0 of Cr(VI) photoreduction using high-entropy $(CeGdSmYZr)O_2$ oxide photocatalyst prepared using various F/O ratio and (b) its corresponding Cr(VI) reduction (%) and rate constant values. (Catalyst: 10 mg/L , Cr(VI): 50 ppm , and formic acid: 500 µl)

3.1.1 Effect of catalyst loading

It is generally believed that the reaction rate in a system is influenced by the concentration of catalysts used in it. To investigate this, different initial photocatalyst concentrations were used for Cr(VI) reduction and the corresponding photoreduction activity including UV-visible spectra, $\ln(C_0/C)$ plots is shown in fig. 6, fig. S7, and fig. S8 respectivly. It is observed that, the percentage removal of Cr(VI) increases with an increase in photocatalyst dosage until optimal photocatalyst concentration of 100mg/L. For a photocatalyst concentration of 25 mg/L, the Cr(VI) reduction of 40.75 % was achieved which increased to 61.46 % for a catalyst loading of 100 mg/L. Increased active sites are responsible for the improved Cr(VI) reduction in the system. Unfortunately, the Cr(VI) reduction is hindered when the catalyst concentration was above 100 mg/L where the least Cr(VI) reduction of 33.17 % was achieved for a catalyst dosage of 500 mg/L. At higher concentrations, the interaction of incident photons with the catalyst is hindered due to the scattering of light photons and poor light penetration through the catalyst surface. Incident photons when interacting with photocatalyst create an electron-hole pair

which is responsible for Cr(VI) reduction. As a result, catalyst overdose hinders this process which significantly decreases the overall Cr(VI) reduction kinetics. The optimum amount of catalyst was therefore determined to be 100 mg/L based on the perspective of cost-effectiveness.

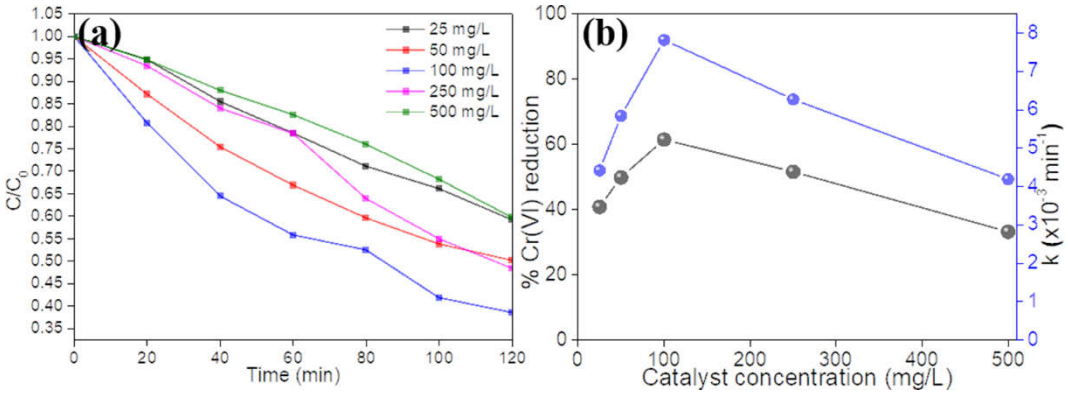

Fig. 6: (a) Effect of photocatalyst concentration on Cr(VI) photoreduction and (b) its corresponding reduction (%) and rate constant values. (Cr(VI): 50 ppm , and formic acid: 500 µl)

3.1.2 Effect of initial Cr(VI) concentration

The performance of the photocatalyst must be evaluated at various Cr(VI) concentrations since industrial wastewater always contains various Cr(VI) concentrations and varies based on the type of industry. Therefore, the effect of the initial Cr(VI) concentration and its reduction efficiency by high-entropy oxide nanoparticles was investigated (fig. 7 and fig. S9) and $\ln(C_0/C)$ plots in fig. S10. It is evident that the photocatalyst performance was better untill a Cr(VI) concentration of 50 ppm and with a further increase in Cr(VI) concentration, the photocatalytic performance plummeted. It is likely that the reduced activity is due to the availability of excess Cr(VI) ions but the number of active site of the photocatalyst is limited which further delays Cr(VI) reduction. A greater percentage of light is intercepted before reaching the catalyst surface, resulting in a decreased photoreduction of Cr(VI)[41]. This

decrease in light availability leads to a decrease in the rate of reaction. Also, it is important to consider the amount of light available for the reaction when considering the environmental impact of Cr(VI) reduction. Therefore the synthesized photocatalyst displays better Cr(VI) reduction only at optimal concentrations and could not perform well at higher Cr(VI) concentrations. This could be improved by employing other strategies and could be a potential research direction.

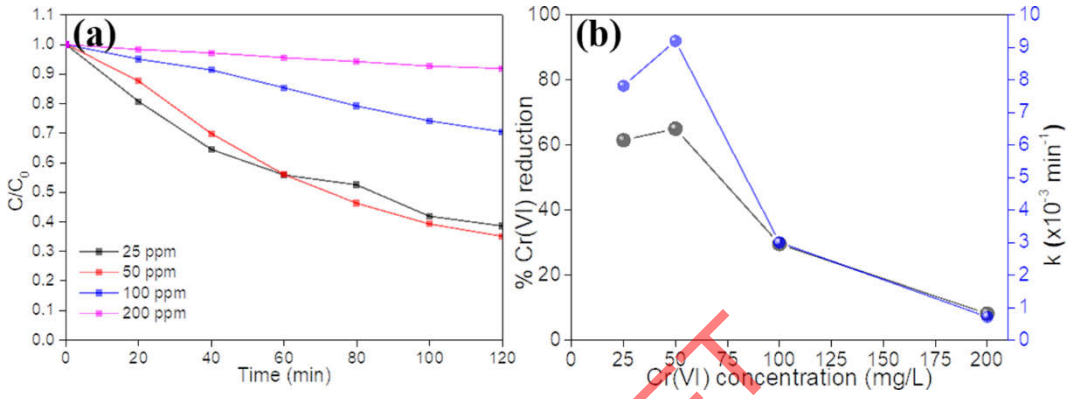

Fig. 7: (a) Effect of initial Cr(VI) concentration and (b) its corresponding photoreduction (%) and rate constant values. (Catalyst: 100 mg/L and formic acid: 500 µl)

3.1.3 Effect of hole scavenger

In general, the electron-hole recombination rate of semiconductor photocatalyst affects the photocatalyst performance especially in Cr(VI) reduction. Faster electron-hole recombination delays the reaction kinetics and this situation can be overcome by either forming heterojunctions or by the addition of hole scavengers. Formic acid is generally used as a hole scavenger which prevents electron-hole recombination[8, 16, 42, 43]. By trapping holes, formic acid inhibits the instant recombination of electrons and holes generated during photon interaction with the photocatalyst, increasing the concentration of available free electrons. As a result, the free electrons available in the conduction band of the semiconductor photocatalyst take part in the catalytic reduction of Cr(VI). In a study, addition of formic acid along with

Ag_2S/RGO/Ag_3PO_4 photocatalyst improved the Cr(VI) reduction because formic acid inhibits the recombination between photoinduced charges[44]. Similarly, the role of formic acid as a hole scavenger was explored in $ZnFe_2O_4$ aerogel photocatalyst[45]. During the photocatalytic reaction, formic acid absorbs the photogenerated holes and forms $\bullet CO_2^-$ thereby improving the Cr(VI) reduction. As a result, the present study examined the role of formic acid in the reduction of Cr(VI). Fig. 8 shows the effect of initial formic acid concentration on photocatalytic Cr(VI) reduction along with UV-visible spectra and ln(C_0/C) plots (fig. S11 and S12). The Cr(VI) reduction is dependent on the concentration of formic acid which relates to the increased hole scavenging ability. Interestingly, near complete Cr(VI) reduction (99.14 %) was achieved when 2 ml of formic acid was added to the photocatalytic reaction with a rate constant of 0.0389 min^{-1}. To compare the current photocatalyst performance, table 2 displays the list of recently reported photocatalysts on Cr(VI) reduction. In most cases, the system comprises heterojunctions formed from metals, oxides, and carbon. But the performance of our photocatalyst which does not contain any noble metals or heterojunction performed better in terms of Cr(VI) reduction. Future investigations will focus on improving the material's photocatalytic properties. This is an open and interesting problem for researchers to address.

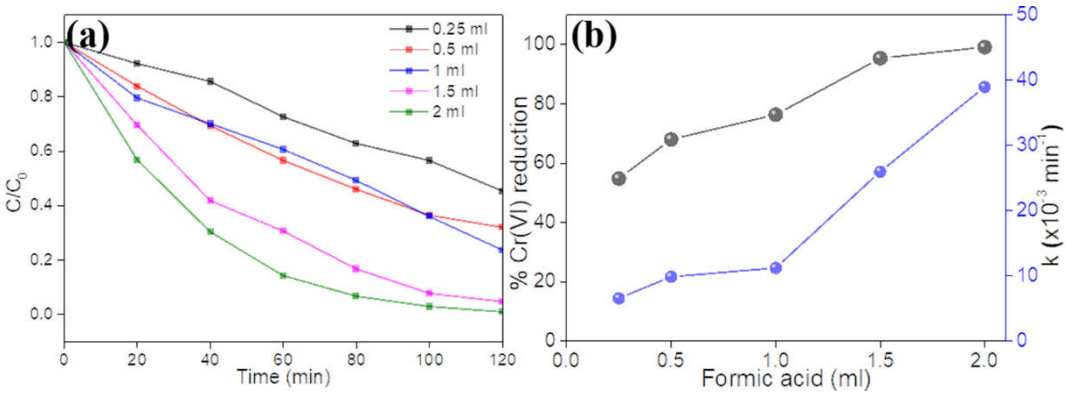

Fig. 8: (a) Effect of formic acid on the photocatalytic reduction of Cr(VI) and (b) its corresponding reduction (%) and rate constant values. (Catalyst: 100 mg/L and Cr(VI): 50 ppm)

Table 2. Comparison of photocatalytic reduction of Cr(VI) with different catalyst with our synthesized high-entropy oxide photocatalyst.

Catalyst	Catalyst concentration	Irradiation source	Cr(VI) concentration	Photoreduction time	% Cr(VI) reduction	Rate constant (min^{-1})	Reference
0D/2D CeO_2/CdS	600 mg/L	300 W Xenon lamp	20 mg/L	40 min	99.94	0.0952	[46]
CeO_2 nanorods /$SnIn_4S_8$	333 mg/L	250 W Xenon lamp	20 mg/L	60 min	94.1	0.0434	[47]
CQDs/HBWO-18	200 mg/L	Xenon lamp	10 mg/L	60 min	88	-	[48]
Ag NPs-modified C–TiO_2/$Cd_{0.5}Zn_{0.5}S$	500 mg/L	500 W Xe lamp	5 mg/L	90 min	94.4	-	[49]
Fe_2O_3@BOC1	1000mg/L	100 W visible light	20 ppm	150 min	100	-	[50]
Bi_2MoO_6 /ZnO	2000 mg/L	300 W (Xe	50 mg/L	150 min	100	0.0135	[51]

		lamp, λ > 400 nm)					
$Ce_{0.2}Gd_{0.2}Hf_{0.2}La_{0.2}Zr_{0.2}O_2$	500 mg/L	Sunlight	100 ppm	90 min	100	0.0175	[8]
$Gd_{0.2}Hf_{0.2}La_{0.2}Y_{0.2}Zr_{0.2}O_2$	500 mg/L	Sunlight	100 ppm	100 min	100	0.0168	[8]
$(CeGdSmYZr)O_2$	100 mg/L	100 W UV-light (365 nm)	50 ppm	120 min	99.14	0.0389	This work

3.1.4 Mechanism of photocatalytic reduction of toxic Cr(VI)

To investigate the photocatalytic mechanism, it is necessary to find the band edge positions of the photocatalyst which determines the reaction kinetics. Based on the reported literature, the valance band (E_V) and conduction band (E_{CB}) position of high-entropy $(CeGdSmYZr)O_2$ oxide photocatalyst was calculated and displayed in Table 1. Clearly, the conduction band position of HEC-1.4 is more negative when compared to other samples which emphasizes the higher photocatalytic reduction of Cr(VI).

Fig. 9 depicts the overall photocatalytic mechanism of Cr(VI) reduction by the high-entropy $(CeGdSmYZr)O_2$ oxide photocatalyst. When the photocatalyst is irradiated with a light source whose energy is higher than the bandgap energy, an electron-hole pair is generated (equation (5)). The energy absorbed by the photocatalyst ejects the electrons (e^-) from the valance band (VB) and the electrons of this type are highly reactive, mobile, and unselective, migrate to the

conduction band (CB) of the photocatalyst. This migration of electrons creates a positive hole species (h^+) in the VB of the photocatalyst. Meanwhile, water molecules interact with the holes and produce $^{\bullet}OH$ and H^+ as displayed in equation (6). Photocatalysts based on semiconductors have limitations in terms of faster electron-hole pair recombination. As a result, the performance of the photocatalysts is limited and the effective method of preventing this is to use a hole scavenger such as formic acid. Formic acid when added reacts with the holes available in the valance band and hydroxyl radicals to produce reactive $\bullet CO_2^-$ thereby suppressing the electron-hole recombination (equation (7)). In the meantime, the main chemical species of Cr(VI) at acidic pH values exist as $HCrO_4^-$ in the reaction solution[52]. This reaction pathway is plausible due to the lower redox potential $E^0(\bullet CO_2^-/CO_2) = -1.9$ V vs. NHE compared to Cr(VI), $E^0(HCrO_4^-/Cr^{3+}) = 1.33$ V vs. NHE. Consequently, the electrons in the conduction band are more readily available for Cr(VI) reduction thus increasing the reduction pathway for Cr(VI). Moreover, the redox potential of Cr(VI) is more positive than the CB position of the photocatalyst facilitating efficient electron transfer to Cr(VI) (equation (8)).

$$(CeGdSmYZr)O_2 + h\nu \rightarrow h_{VB}^+ + e_{CB}^- \quad (5)$$

$$H_2O + h_{VB}^+ \rightarrow {}^{\bullet}OH + H^+ \quad (6)$$

$$HCOOH + {}^{\bullet}OH \rightarrow {}^{\bullet}CO_2^- + H_3O^+ \quad (7)$$

$$HCrO_4^- + 7H^+ + 3e_{CB}^- \rightarrow Cr^{3+} + 4H_2O \quad (8)$$

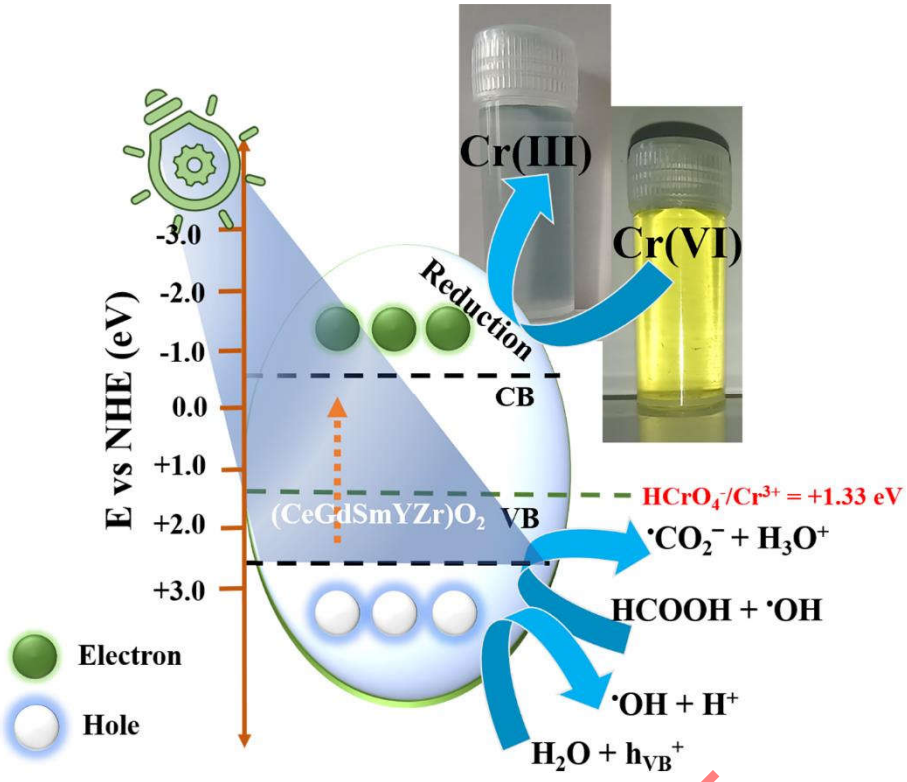

Fig. 9: Photocatalytic reduction mechanism of high-entropy $(CeGdSmYZr)O_2$ oxide photocatalyst for the reduction of toxic Cr(VI) to less toxic Cr(III) in the presence of formic acid.

To investigate the recombination behaviour of all the synthesized high entropy $(CeGdSmYZr)O_2$ oxide photocatalyst, PL spectra were recorded and is depicted in Fig. 10. The intensity of PL emission determines the separation ability of photoexcited electron–hole (e^--h^+) pairs which is a crucial factor in determining the reaction kinetics[18]. The PL emission spectrum was maximum for the HEC-0.6 sample representing a faster recombination rate. PL emission intensity was affected by synthesis conditions, with sample HEC-1.4 having the least PL emission intensity. Therefore, in the case of the HEO-1.4 sample, delayed (e^--h^+) pair recombination improved the photocatalytic reduction of Cr(VI).

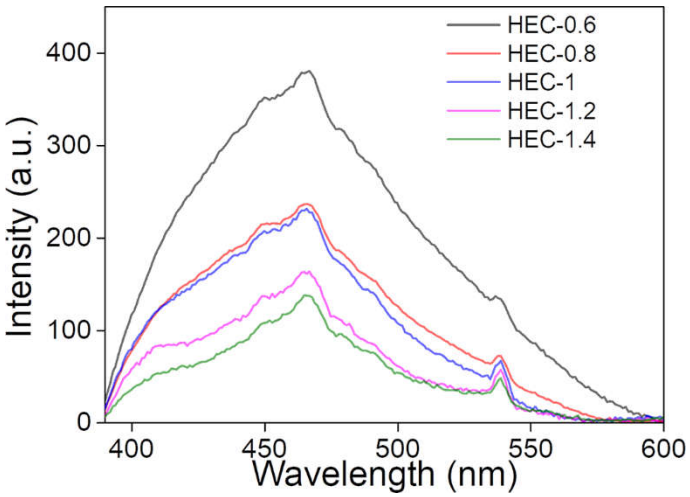

Fig. 10: Photoluminescence emission spectra of different high-entropy $(CeGdSmYZr)O_2$ oxide samples.

It is important to consider the stability of a photocatalyst when determining its efficiency and cost-effectiveness. The performance and stability of a high-entropy $(CeGdSmYZr)O_2$ oxide photocatalyst was evaluated over a period of 5 cycles and the result was presented in fig. 11(a) and (b). Following the first run, the high-entropy $(CeGdSmYZr)O_2$ oxide photocatalyst was separated from the reaction solution by centrifuge and washed with distilled water. The washed photocatalyst was used as such for the subsequent cycles without drying. The photocatalyst performed better in all five consecutive cycles and the Cr(VI) reduction fell by 9.66 % at the end of the fifth cycle. This decline is due to the loss of photocatalyst during the recovery step which involves washing. Apart from this, to check the phase stability of the recycled photocatalyst, xrd analysis was carried out and the result is displayed in fig. 11(c). The xrd results confirm the presence of single-phase cubic fluorite oxide without any phase separation which possesses excellent phase and structural stability. In addition, FTIR spectra were recorded on the freshly prepared and spent photocatalyst (Fig. 11(d)). It is evident that both the spent and new photocatalysts exhibit similar vibrational behaviour and no additional vibrations are barely visible.

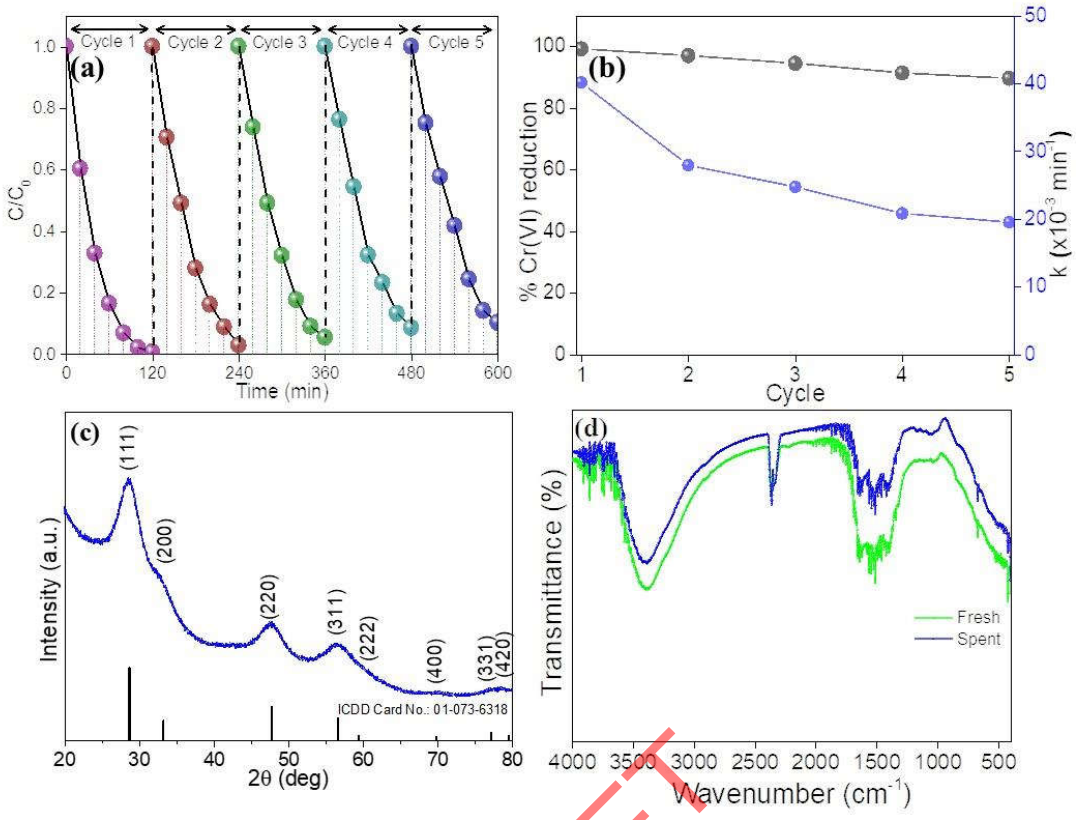

Fig: 11. (a) Recyclability test for the photocatalytic reduction of Cr(VI) solution using (CeGdSmYZr)O_2 catalyst illuminated under UV-light source and (b) its corresponding reduction (%) and rate constant values. (Catalyst: 100 mg/L; Cr(VI): 50 ppm; Formic acid: 2 ml), (c) XRD pattern of spent catalyst and (d) FTIR spectra of fresh and spent catalyst.

The xrd and FTIR results confirm the high stability and structural integrity of the prepared high-entropy (CeGdSmYZr)O_2 oxide photocatalyst. Hence, based on the results of the present study, the photocatalyst could be applied to other applications, such as hydrogen production, or as a catalyst in other chemical reactions.

4. Conclusion

A reusable high-entropy (CeGdSmYZr)O_2 oxide photocatalyst was prepared using a simple solution combustion synthesis. Various (CeGdSmYZr)O_2 oxide samples were prepared by varying the fuel-to-oxidizer ratio. All synthesized high-entropy (CeGdSmYZr)O_2 oxides form

a single-phase pure structure in a cubic fluorite structure. All the samples exhibit a porous structure and based on the synthesis conditions; the photocatalytic reduction of Cr(VI) is affected. Better Cr(VI) reduction is achieved for samples prepared at fuel-rich conditions (HEC-1.4) due to the small crystallite size and high surface area values. Moreover, the performance of the photocatalyst is dependent on several parameters while the concentration of formic acid enhances Cr(VI) reduction. This is possible due to the suppression of holes present in the photocatalyst valance band. The current $(CeGdSmYZr)O_2$ photocatalyst is both chemically and structurally stable making it a suitable photocatalyst material. Apart from the photocatalytic properties, the high entropy oxide can be used as a UV-blocker due to its high spectral absorbance in the UV region.

Acknowledgements

The study was supported by the Russian Science Foundation grant No. 23-73-10139, https://rscf.ru/project/23-73-10139/

References:

[1] A. Saravanan, P.S. Kumar, S. Jeevanantham, M. Anubha, S. Jayashree, Degradation of toxic agrochemicals and pharmaceutical pollutants: Effective and alternative approaches toward photocatalysis, Environmental Pollution, 298 (2022) 118844.

[2] A. Intisar, A. Ramzan, T. Sawaira, A.T. Kareem, N. Hussain, M.I. Din, et al., Occurrence, toxic effects, and mitigation of pesticides as emerging environmental pollutants using robust nanomaterials – A review, Chemosphere, 293 (2022) 133538.

[3] M.E. Hossain, S. Shahrukh, S.A. Hossain, Chemical Fertilizers and Pesticides: Impacts on Soil Degradation, Groundwater, and Human Health in Bangladesh, in: V.P. Singh, S. Yadav, K.K. Yadav, R.N. Yadava (Eds.) Environmental Degradation: Challenges and Strategies for Mitigation, Springer International Publishing, Cham, 2022, pp. 63-92.

[4] P. Sharma, H.M.N. Iqbal, R. Chandra, Evaluation of pollution parameters and toxic elements in wastewater of pulp and paper industries in India: A case study, Case Studies in Chemical and Environmental Engineering, 5 (2022) 100163.

[5] M. Nigam, P. Mishra, P. Kumar, S. Rajoriya, P. Pathak, S.R. Singh, et al., Comprehensive technological assessment for different treatment methods of leather tannery wastewater, Environmental Science and Pollution Research, (2022).

[6] K.K. Sodhi, L.C. Mishra, C.K. Singh, M. Kumar, Perspective on the heavy metal pollution and recent remediation strategies, Current Research in Microbial Sciences, 3 (2022) 100166.

[7] E.C. Emenike, K.O. Iwuozor, S.U. Anidiobi, Heavy Metal Pollution in Aquaculture: Sources, Impacts and Mitigation Techniques, Biological Trace Element Research, 200 (2022) 4476-4492.

[8] M. Anandkumar, A. Lathe, A.M. Palve, A.S. Deshpande, Single-phase $Gd_{0.2}La_{0.2}Ce_{0.2}Hf_{0.2}Zr_{0.2}O_2$ and $Gd_{0.2}La_{0.2}Y_{0.2}Hf_{0.2}Zr_{0.2}O_2$ nanoparticles as efficient photocatalysts for the reduction of Cr(VI) and degradation of methylene blue dye, Journal of Alloys and Compounds, 850 (2021) 156716.

[9] M.M. Ali, M.S. Islam, A.R.M.T. Islam, M.S. Bhuyan, A.S.S. Ahmed, M.Z. Rahman, et al., Toxic metal pollution and ecological risk assessment in water and sediment at ship breaking sites in the Bay of Bengal Coast, Bangladesh, Marine Pollution Bulletin, 175 (2022) 113274.

[10] G. Qin, Z. Niu, J. Yu, Z. Li, J. Ma, P. Xiang, Soil heavy metal pollution and food safety in China: Effects, sources and removing technology, Chemosphere, 267 (2021) 129205.

[11] U. Okereafor, M. Makhatha, L. Mekuto, N. Uche-Okereafor, T. Sebola, V. Mavumengwana, Toxic Metal Implications on Agricultural Soils, Plants, Animals, Aquatic life and Human Health, International Journal of Environmental Research and Public Health, 17 (2020) 2204.

[12] P. Sharma, S.P. Singh, S.K. Parakh, Y.W. Tong, Health hazards of hexavalent chromium (Cr (VI)) and its microbial reduction, Bioengineered, 13 (2022) 4923-4938.

[13] A. Basaleh, A.A. Ismail, R.M. Mohamed, Novel visible light heterojunction CdS/Gd_2O_3 nanocomposites photocatalysts for Cr(VI) photoreduction, Journal of Alloys and Compounds, 927 (2022) 166988.

[14] N.A. Azeez, S.S. Dash, S.N. Gummadi, V.S. Deepa, Nano-remediation of toxic heavy metal contamination: Hexavalent chromium [Cr(VI)], Chemosphere, 266 (2021) 129204.

[15] K. Zhang, Y. Fu, D. Hao, J. Guo, B.-J. Ni, B. Jiang, et al., Fabrication of CN75/NH_2-MIL-53(Fe) p-n heterojunction with wide spectral response for efficiently photocatalytic Cr(VI) reduction, Journal of Alloys and Compounds, 891 (2022) 161994.

[16] A. Lathe, A.M. Palve, A review: Engineered nanomaterials for photoreduction of Cr(VI) to Cr(III), Journal of Hazardous Materials Advances, 12 (2023) 100333.

[17] H. Karimi-Maleh, A. Ayati, S. Ghanbari, Y. Orooji, B. Tanhaei, F. Karimi, et al., Recent advances in removal techniques of Cr(VI) toxic ion from aqueous solution: A comprehensive review, Journal of Molecular Liquids, 329 (2021) 115062.

[18] M. Anandkumar, E. Trofimov, Synthesis, Properties, and Applications of High-Entropy Oxide Ceramics: Current Progress and Future Perspectives, Journal of Alloys and Compounds, (2023) 170690.

[19] V.R. Naganaboina, M. Anandkumar, A.S. Deshpande, S.G. Singh, Single-Phase High-Entropy Oxide Nanoparticles for Wide Dynamic Range Detection of CO_2, ACS Applied Nano Materials, 5 (2022) 4524-4536.

[20] V.R. Naganaboina, S. Bonam, M. Anandkumar, A.S. Deshpande, S.G. Singh, Humidity-Independent Methane Gas Detection in $Gd_{0.2}La_{0.2}Ce_{0.2}Hf_{0.2}Zr_{0.2}O$□-Based Sensor Using Polynomial Regression Analysis, IEEE Electron Device Letters, 43 (2022) 2153-2156.

[21] M. Anandkumar, S. Bhattacharya, A.S. Deshpande, Low temperature synthesis and characterization of single phase multi-component fluorite oxide nanoparticle sols, RSC Advances, 9 (2019) 26825-26830.

[22] V.R. Naganaboina, M. Anandkumar, A.S. Deshpande, S.G. Singh, Single-phase high-entropy oxide-based chemiresistor: Toward selective and sensitive detection of methane gas for real-time applications, Sensors and Actuators B: Chemical, 357 (2022) 131426.

[23] M. Anandkumar, P.M. Bagul, A.S. Deshpande, Structural and luminescent properties of Eu^{3+} doped multi-principal component $Ce_{0.2}Gd_{0.2}Hf_{0.2}La_{0.2}Zr_{0.2}O_2$ nanoparticles, Journal of Alloys and Compounds, 838 (2020) 155595.

[24] A. Sarkar, C. Loho, L. Velasco, T. Thomas, S.S. Bhattacharya, H. Hahn, et al., Multicomponent equiatomic rare earth oxides with a narrow band gap and associated praseodymium multivalency, Dalton Transactions, 46 (2017) 12167-12176.

[25] P. Edalati, Y. Itagoe, H. Ishihara, T. Ishihara, H. Emami, M. Arita, et al., Visible-light photocatalytic oxygen production on a high-entropy oxide by multiple-heterojunction introduction, Journal of Photochemistry and Photobiology A: Chemistry, 433 (2022) 114167.

[26] M. Ismael, Latest progress on the key operating parameters affecting the photocatalytic activity of TiO_2-based photocatalysts for hydrogen fuel production: A comprehensive review, Fuel, 303 (2021) 121207.

[27] N.S. Ibrahim, W.L. Leaw, D. Mohamad, S.H. Alias, H. Nur, A critical review of metal-doped TiO_2 and its structure–physical properties–photocatalytic activity relationship in hydrogen production, International Journal of Hydrogen Energy, 45 (2020) 28553-28565.

[28] Y. Hu, M. Anandkumar, J. Joardar, X. Wang, A.S. Deshpande, K.M. Reddy, Effective band gap engineering in multi-principal oxides (CeGdLa-Zr/Hf)Ox by temperature-induced oxygen vacancies, Scientific Reports, 13 (2023) 2362.

[29] W. Ren, J. Yang, J. Zhang, W. Li, C. Sun, H. Zhao, et al., Recent progress in SnO_2/g-C_3N_4 heterojunction photocatalysts: Synthesis, modification, and application, Journal of Alloys and Compounds, 906 (2022) 164372.

[30] F. Siddique, S. Gonzalez-Cortes, A. Mirzaei, T. Xiao, M.A. Rafiq, X. Zhang, Solution combustion synthesis: the relevant metrics for producing advanced and nanostructured photocatalysts, Nanoscale, 14 (2022) 11806-11868.

[31] H. Nasiri, E. Bahrami Motlagh, J. Vahdati Khaki, S.M. Zebarjad, Role of fuel/oxidizer ratio on the synthesis conditions of Cu–Al_2O_3 nanocomposite prepared through solution combustion synthesis, Materials Research Bulletin, 47 (2012) 3676-3680.

[32] C.S. Naveen, M.L. Dinesha, H.S. Jayanna, Effect of Fuel to Oxidant Molar Ratio on Structural and DC Electrical Conductivity of ZnO Nanoparticles Prepared by Simple Solution Combustion Method, Journal of Materials Science & Technology, 29 (2013) 898-902.

[33] M. Anandkumar, G. Vinothkumar, K. Suresh Babu, Synergistic effect of gold supported on redox active cerium oxide nanoparticles for the catalytic hydrogenation of 4-nitrophenol, New Journal of Chemistry, 41 (2017) 6720-6729.

[34] B.N. Sherikar, B. Sahoo, A.M. Umarji, Effect of fuel and fuel to oxidizer ratio in solution combustion synthesis of nanoceramic powders: MgO, CaO and ZnO, Solid State Sciences, 109 (2020) 106426.

[35] S. Hadke, M.T. Kalimila, S. Rathkanthiwar, S. Gour, R. Sonkusare, A. Ballal, Role of fuel and fuel-to-oxidizer ratio in combustion synthesis of nano-crystalline nickel oxide powders, Ceramics International, 41 (2015) 14949-14957.

[36] E. Carlos, R. Martins, E. Fortunato, R. Branquinho, Solution Combustion Synthesis: Towards a Sustainable Approach for Metal Oxides, Chemistry – A European Journal, 26 (2020) 9099-9125.

[37] S.L. González-Cortés, F.E. Imbert, Fundamentals, properties and applications of solid catalysts prepared by solution combustion synthesis (SCS), Applied Catalysis A: General, 452 (2013) 117-131.

[38] W. Kang, D.O. Ozgur, A. Varma, Solution Combustion Synthesis of High Surface Area CeO_2 Nanopowders for Catalytic Applications: Reaction Mechanism and Properties, ACS Applied Nano Materials, 1 (2018) 675-685.

[39] B. Pourgolmohammad, S.M. Masoudpanah, M.R. Aboutalebi, Synthesis of $CoFe_2O_4$ powders with high surface area by solution combustion method: Effect of fuel content and cobalt precursor, Ceramics International, 43 (2017) 3797-3803.

[40] J.J. Testa, M.A. Grela, M.I. Litter, Experimental Evidence in Favor of an Initial One-Electron-Transfer Process in the Heterogeneous Photocatalytic Reduction of Chromium(VI) over TiO_2, Langmuir, 17 (2001) 3515-3517.

[41] M. Valari, A. Antoniadis, D. Mantzavinos, I. Poulios, Photocatalytic reduction of Cr(VI) over titania suspensions, Catalysis Today, 252 (2015) 190-194.

[42] V. Hasija, P. Raizada, P. Singh, N. Verma, A.A.P. Khan, A. Singh, et al., Progress on the photocatalytic reduction of hexavalent Cr (VI) using engineered graphitic carbon nitride, Process Safety and Environmental Protection, 152 (2021) 663-678.

[43] F. Besharat, F. Ahmadpoor, M. Nasrollahzadeh, Graphene-based (nano)catalysts for the reduction of Cr(VI): A review, Journal of Molecular Liquids, 334 (2021) 116123.

[44] S.M. Abdo, S.I. El-Hout, M.N. Rashed, T.I. El-Dosoqy, S.M. El-Sheikh, Modified silver phosphate nanocomposite as an effective visible-light-driven photocatalyst in the reduction of aqueous Cr(VI), Materials Research Bulletin, 169 (2024) 112511.

[45] S.-t. Huang, J.-x. Tai, W.-k. Hao, J.-x. Lu, S.-j. Liu, X.-d. Wu, et al., A novel magnetic $ZnFe_2O_4$ aerogel photocatalyst for visible light reduction of Cr(VI) at high concentrations:

Facile synthesis, enhanced activity and photocatalytic mechanism, combined with first-principles calculations, Ceramics International, 48 (2022) 3974-3984.

[46] H. Yin, C. Yuan, H. Lv, X. Chen, K. Zhang, Y. Zhang, Construction of 0D/2D CeO_2/CdS direct Z-scheme heterostructures for effective photocatalytic H_2 evolution and Cr(VI) reduction, Separation and Purification Technology, 295 (2022) 121294.

[47] Y. Xiao, Y. Tao, Y. Jiang, J. Wang, W. Zhang, Y. Liu, et al., Construction of core–shell CeO_2 nanorods/$SnIn_4S_8$ nanosheets heterojunction with rapid spatial electronic migration for effective wastewater purification and H_2O_2 production, Separation and Purification Technology, 304 (2023) 122385.

[48] C. Li, Z. Zhao, S. Fu, X. Wang, Y. Ma, S. Dong, Polyvinylpyrrolidone in the one-step synthesis of carbon quantum dots anchored hollow microsphere Bi_2WO_6 enhances the simultaneous photocatalytic removal of tetracycline and Cr (VI), Separation and Purification Technology, 270 (2021) 118844.

[49] Y. Wang, C. Kang, X. Li, Q. Hu, C. Wang, Ag NPs decorated C–TiO_2/$Cd_{0.5}Zn_{0.5}S$ Z-scheme heterojunction for simultaneous RhB degradation and Cr(VI) reduction, Environmental Pollution, 286 (2021) 117305.

[50] P. Kar, P. Jain, V. Kumar, R.K. Gupta, Interfacial engineering of Fe_2O_3@BOC heterojunction for efficient detoxification of toxic metal and dye under visible light illumination, Journal of Environmental Chemical Engineering, 7 (2019) 102843.

[51] G. Zhang, D. Chen, N. Li, Q. Xu, H. Li, J. He, et al., Fabrication of Bi_2MoO_6/ZnO hierarchical heterostructures with enhanced visible-light photocatalytic activity, Applied Catalysis B: Environmental, 250 (2019) 313-324.

[52] J.B. Islam, M. Furukawa, I. Tateishi, H. Katsumata, S. Kaneco, Photocatalytic Reduction of Hexavalent Chromium with Nanosized TiO_2 in Presence of Formic Acid, ChemEngineering, 3 (2019) 33.